

Universidad Carlos III de Madrid



Institutional Repository

This document is published in:

Journal of Alloys and Compounds (2014). 595, 1-7.

DOI: <http://dx.doi.org/10.1016/j.jallcom.2014.01.091>

© 2014 Elsevier B.V.

Hot workability of nanocrystalline AZ91 magnesium alloy

M.A. Jabbari-Taleghani ^{*}, J.M. Torralba

Department of Materials Science and Engineering, Universidad Carlos III de Madrid, Avda. de la Universidad 30, 28911 Leganés, Madrid, Spain
IMDEA Materials Institute, C/ Eric Kandel 2, Technoetafe, 28906 Getafe, Madrid, Spain

^{*}Corresponding author at: Department of Materials Science and Engineering, Universidad Carlos III de Madrid, Avda. de la Universidad 30, 28911 Leganés, Madrid, Spain. Tel.: +34 91 5493422; fax: +34 91 5503047. E-mail address: mohammad.jabbari@imdea.org (M.A. Jabbari-Taleghani).

Abstract: This study examined the hot deformation behavior and workability characteristics of nanocrystalline AZ91 Mg alloy by performing hot compression tests with a Gleeble-3800 machine. To this end, a nano-crystalline alloy powder with a crystallite size of 25 nm was synthesized via mechanical milling of a pre-alloyed AZ91 Mg alloy powder for 14 h. The mechanically milled (MM) AZ91 powder was subsequently cold pressed at 600 MPa into cylindrical compacts measuring 10 mm in diameter and 12 mm in height. Then, the powder compacts with a relative green density of 91% were hot-compressed at temperatures ranging from 150 °C to 500 °C and at true strain rates ranging from 0.001 s⁻¹ to 10 s⁻¹. The true stress-true strain curves peaked at low strains, after which the flow stress increased moderately. Processing maps were developed for all of the hot compression tests at strains of 0.1, 0.5, and 0.8, which represented a safe deformation domain at deformation temperatures and strain rates in the ranges of 250–350 °C and 0.1–10 s⁻¹. The crystallite size of the nanocrystalline AZ91 Mg alloy hot-compressed within the aforementioned domain was measured to be 140 nm, which is considered very fine for Mg alloys and resulted in a high hardness value of 133 HV for the hot-compressed alloy.

Keywords: Nanocrystalline magnesium alloys, Mechanical milling, Hot compression test, Hot deformation behavior, Processing map, Workability.

1. Introduction

Mg alloys have received considerable attention as a structural material in recent years due to their interesting properties, such as low density, high strength-to-weight ratio, good damping characteristics, superior machinability, and excellent castability [1,2]. To date, most of the research and development on Mg alloys has been performed by the automotive industry; and die casting has been the main manufacturing route for Mg products because of the poor workability of Mg at room temperature, which is a result of its HCP crystal structure [3]. However, die cast Mg products have considerable disadvantages, such as pin holes, porosity, cold shuts, and low strength. In fact, the market for Mg products continues to grow, but many opportunities remain untapped because of the relatively low stiffness and strength of these products. Due to the limited number of slip systems of Mg and its correspondingly large Taylor factor, grain refinement remarkably improves the mechanical properties of Mg and its alloys. It is well known that the fine-grained Mg alloys exhibit an interesting combination of high strength and high ductility at room temperature and superplasticity at elevated temperatures [4]. Superplastic flow occurs by grain boundary sliding, with the sliding accommodated by some limited dislocation slip in the adjacent grains [5]. Consequently, the processing of fine-grained Mg alloys has drawn great interests in the past few years.

Mechanical properties of Mg alloys can effectively be improved by refining their grain structures through dynamic recrystallization (DRX), which generally occurs during hot deformation of these materials. Recently, grain refinement due to DRX during hot deformation has been demonstrated in pure Mg [6] and in conventional wrought Mg alloys such as Mg–Al–Zn [7–9] and Mg–Zn–Zr alloys [10,11]. The grain sizes of different Mg alloys processed by conventional forming processes, such as extrusion and rolling, and also by severe plastic deformation techniques, such as equal channel angular pressing (ECAP) and high pressure torsion (HPT), have been reported to range from 800 nm to 20 μm. However, it has been well established that nanocrystalline metallic alloys with grain sizes less than 100 nm generally exhibit significantly improved mechanical properties over their microcrystalline counterparts. So far, most of the research work on nanocrystalline materials has been carried out on face-centered cubic (FCC) and body-centered cubic (BCC) metals, and studies on nanocrystalline Mg alloys are relatively scarce.

Mechanical milling has proven to be an effective technique for processing nanocrystalline metallic alloys. Most of the previous works on the mechanical milling of Mg alloys concern the processing of Mg matrix composites [12–14] and high performance Mg-based hydrogen storage alloys [15–17]. A number of studies have also examined the microstructural characteristics, thermal

stability, and mechanical properties of nanocrystalline Mg alloys processed by mechanical milling. It has been reported that the grain sizes of Mg and its alloys can be refined to 30–50 nm through mechanical milling, and nanocrystalline Mg alloys produced by high-energy milling show excellent resistance to grain growth during isothermal annealing and/or subsequent consolidation processes at high temperatures, leading to superior mechanical properties for the bulk alloys consolidated from mechanically milled Mg-based powders [18–22].

The powders processed by mechanical milling are then consolidated by powder metallurgy (PM) routes, such as cold pressing and sintering, powder extrusion, powder forging, and powder rolling. The surfaces of Mg-based powders are covered with a thin stable oxide layer, which strongly inhibits sintering of these powders. Hence, the sintering of Mg-based powders is generally regarded as unfeasible and problematic [23]. Compared with other PM routes such as sintering and hot pressing, the shear stresses involved in powder extrusion and powder forging make them ideal processes for the production of bulk Mg products from powder mixtures [24]. These shear stresses break the oxide layer covering the particle surfaces of Mg-based powders, which can lead to a well-bonded microstructure and superior after-consolidation mechanical properties. A good understanding of the hot deformation behavior of a material is extremely important in hot deformation processes such as extrusion and forging [25]. Thus, several studies have been performed to investigate the effect of processing parameters on the hot deformation behavior of microcrystalline Mg alloys.

Among all of the existing Mg alloys, AZ91 is the most widely used alloy in industry [26]. However, studies on the hot deformation behavior of AZ91 alloy are relatively scarce; and very limited data are available on this alloy's workability characteristics [27–29]. Furthermore, there are no systematic studies on the hot deformation behavior of nanocrystalline Mg alloys. Therefore, this study focused on the hot deformation behavior and workability characteristics of nanocrystalline AZ91 Mg alloy with a view to finding the optimum hot working parameters and evaluating the mechanisms of hot deformation. For this purpose, the approach of processing map has been adopted.

The processing map technique used in this study is based on the dynamic materials model (DMM), and the efficiency of the power dissipation (η) through microstructural changes during deformation is given by [30]:

$$\eta = 2m/(m + 1) \quad (1)$$

$$m = (\partial \log \sigma)/(\partial \log \dot{\varepsilon}) \quad (2)$$

where m is the strain rate sensitivity of flow stress, σ is the flow stress, and $\dot{\varepsilon}$ is the strain rate. The extremum principles of irreversible thermodynamics as applied to the continuum mechanics of large plastic flow were explored to define a criterion for the onset of flow instability, given by:

$$\xi = (\partial \ln[m/(m + 1)]/\partial \ln \dot{\varepsilon}) + m \leq 0 \quad (3)$$

2. Experimental procedure

The raw material used for this study was a pre-alloyed Mg–Al–Zn powder (Ecka Granules, Germany) with a chemical composition equivalent to that of AZ91 D Mg alloy (8.8 wt% Al, 0.6 wt% Zn, 0.2 wt% Mn, 0.03 wt% Si, and the balance Mg). The mentioned powder was mechanically milled in a horizontal attritor mill (CM01 Simoloyer, ZOZ, Germany) using the following milling parameters: ball-to-powder weight ratio: 20/1; ball diameter: 5 mm; ball material: AISI 420 stainless steel; milling time: 14 h; milling speed: 700 rpm; and milling atmosphere: Ar. Stearic acid (2 wt%) was also employed as the process control agent (PCA).

The mechanically milled (MM) AZ91 powder was uniaxially cold pressed at 600 MPa into cylindrical billets measuring 10 mm in diameter and 12 mm in height using no pressing lubricant. The green densities of the powder compacts were measured to be 91% of the theoretical value, or 1.80 g/cm³.

A graphite foil with a thickness of 0.05 mm was placed between the ends of the powder compacts and the anvils to minimize friction during the hot compression test. Prior to the hot compression tests, the samples were resistance heated in an Ar. atmosphere to the required temperature at a heating rate of 3 °C s⁻¹, then maintained at the test temperature for 1 min to minimize thermal gradients along the sample. Single-hit compression tests were performed using a servo-controlled Gleeble-3800 system (Dynamic Systems Inc., USA) at strain rates of 0.001 s⁻¹, 0.01 s⁻¹, 0.1 s⁻¹, 1 s⁻¹, and 10 s⁻¹ and deformation temperatures ranging from 150 °C to 500 °C, which cover the entire hot working range of Mg alloys. After hot compression, the samples were air-quenched to room temperature. The load–stroke data were converted into true stress–true strain curves using standard equations, which in turn used to compute the efficiency (η) and instability (ξ) parameters as a function of temperature and strain rate.

Scanning electron microscopy (SEM) and X-ray diffractometry (XRD) were employed for the characterization of the as-received and MM AZ91 powders. Besides, differential scanning calorimetry (DSC) study was conducted on the MM AZ91 powder using a simultaneous thermal analyzer (STA) 6000 manufactured by Perkin–Elmer. The MM AZ91 powder was heated in an alumina pan at a rate of 5 °C/min up to 500 °C under flowing Ar. For baseline subtraction, the empty alumina pan was initially tested in the same fashion.

The densities of the compacts hot-compressed to different strain levels were measured by the Archimedes method in accordance with the MPIF 42 standard. The relative densities of hot-compressed specimens were calculated by dividing the measured densities by the theoretical density of MM AZ91 powder, i.e. 1.8 g/cm³. The hot-compressed specimens were then sectioned in the center parallel to the compression direction for the microstructural and mechanical characterization. The sectioned samples were then ground, polished, and examined using SEM, XRD, and Vickers hardness testing (HV1).

3. Results and discussion

3.1. Starting microstructure

Fig. 1(a) illustrates the cross-section microstructure of an AZ91 Mg alloy powder particle, showing that the microstructure of the as-received AZ91 powder was comprised of a dark grey matrix in which a grey precipitate was randomly distributed. The EDS analyses (data not shown) determined that the dark grey matrix was enriched in Mg while the grey precipitate was enriched in Mg and Al. As the atomic numbers of Mg and Al are 12 and 13 respectively, SEM in backscattered electron (BSE) mode was not capable of making an obvious contrast between the matrix of powder particle and the precipitate containing Al. As a result, the grey precipitate is highlighted using a black oval. After the milling process, no second phase precipitates were visible in the microstructure of the MM AZ91 powder (Fig. 1(b)), and the particles of the MM AZ91 powder possessed a grey matrix with no specific microstructural feature.

The XRD patterns of AZ91 and MM AZ91 powders are presented in Fig. 2. The microstructure of AZ91 powder particles was composed of the β -Mg₁₇Al₁₂ precipitates and the α -Mg solid solution matrix. This structure is typical of AZ91 castings [31]. The diffraction peaks of the β -Mg₁₇Al₁₂ phase are barely detectable in the XRD pattern of MM AZ91 powder, which can be related to the dissolution of the β -Mg₁₇Al₁₂ phase in the α -Mg matrix of the powder particles. Another possibility is that mechanical milling caused the β -Mg₁₇Al₁₂ phase to be refined into very fine dispersoids distributed in the α -Mg phase, which are hardly detectable by XRD. The milling process was also found out to affect the intensities and widths of the diffraction peaks of the α -Mg phase, and the mentioned peaks became weaker and wider through mechanical milling. This phenomenon can be attributed to the reduction in particle size, the refinement of crystallite size, and the enhancement of lattice strain, all promoted by the severe plastic deformation of AZ91 powder particles during mechanical milling. The grain sizes of AZ91 casting products normally range between 10 μ m and 150 μ m [31,32]. The AZ91 powder used for this study had been

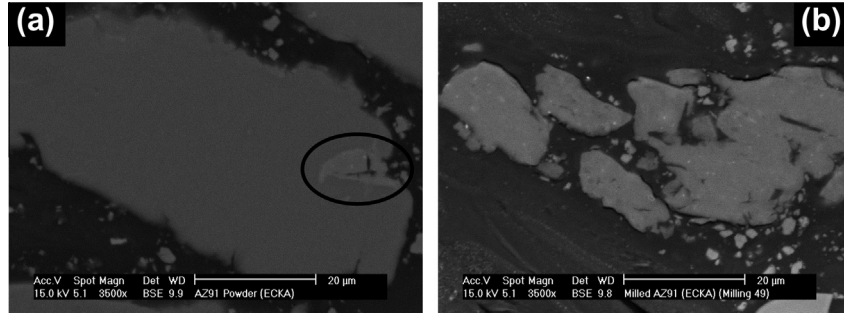


Fig. 1. Microstructure of the cross-section of (a) as-received AZ91 and (b) MM AZ91 powders.

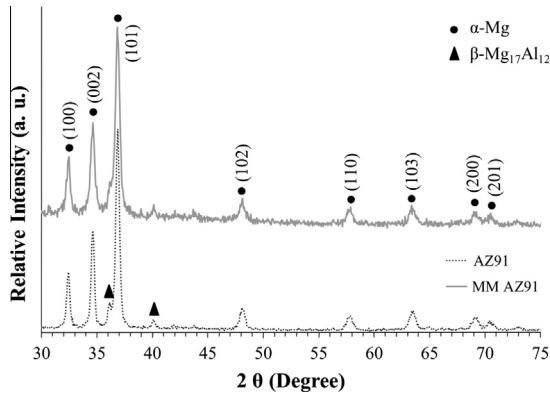


Fig. 2. The XRD patterns of AZ91 (dotted) and MM AZ91 (solid) powders.

produced by the mechanical grinding of AZ91 casting ingots. Considering the production method and the average particle size of the employed AZ91 powder (105 μm), it can be concluded that the grains of this powder should have had micrometer dimensions. The crystallite size of MM AZ91 powder was measured to be 25 nm using the Williamson–Hall method [33], which is in good agreement with those previously reported for high-energy milled Mg-based powders [20,21]. Various models have been proposed to describe the mechanism of formation of nanostructures by high-energy milling [34].

3.2. Flow stress curves

The true stress–true strain curves obtained at deformation temperatures of 200 $^{\circ}\text{C}$, 350 $^{\circ}\text{C}$, and 450 $^{\circ}\text{C}$ and at different strain rates are shown in Fig. 3(a–c) respectively, and represent typical deformation behavior at low ($T \leq 200$ $^{\circ}\text{C}$), moderate (250 $^{\circ}\text{C} \leq T \leq 400$ $^{\circ}\text{C}$), and high deformation temperatures ($T = 450$ $^{\circ}\text{C}$).

In general, the true stress–true strain curves exhibited a peak at low strain values, after which the flow stress increased moderately. In fact, the true stress–true strain curves were of flow hardening type. The specimens cracked at deformation temperatures higher than or equal to 400 $^{\circ}\text{C}$ and at every strain rate, leading to a lower work hardening rate for these specimens. The specimens again cracked or fragmented at a strain rate of 10 s^{-1} and low deformation temperatures, which resulted in a sharp or gradual drop in the flow stress after its peak. As a general trend, as the deformation temperature increased or the strain rate decreased, a decrease in the flow stress level was observed. However, this trend was reverse at some deformation conditions.

During the deformation of porous materials at high temperatures, hardening mechanisms, such as strain and densification hardening, and softening mechanisms, such as dynamic recovery

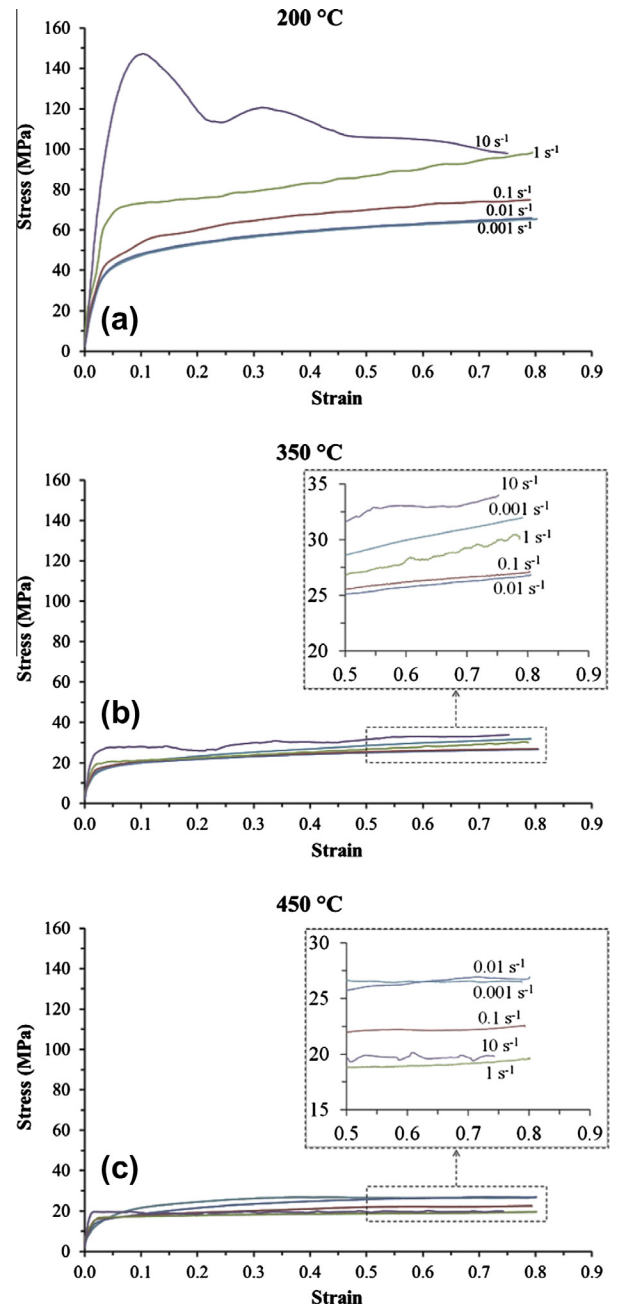


Fig. 3. True stress–true strain curves of the MM AZ91 powder compacts hot-compressed at deformation temperatures of (a) 200 $^{\circ}\text{C}$, (b) 350 $^{\circ}\text{C}$, and (c) 450 $^{\circ}\text{C}$ and at different strain rates.

and recrystallization, can occur simultaneously. At the beginning of deformation, the dislocation density increases rapidly, which leads to a sharp increase in the flow stress (severe work hardening). As deformation continues, the activation of dynamic softening mechanisms can partially or completely neutralize the effect of hardening mechanisms. As a result, the slope of the flow stress flattens and may even become zero or negative.

3.3. Processing maps

The processing maps developed for strains of 0.1, 0.5, and 0.8 are shown in Fig. 4. The contour numbers in these figures represent the efficiency of the power dissipation through dynamic metallurgical mechanisms (η); and the hatched regions represent regions of flow instability, where the instability parameter (ξ) is negative. The regions labeled “Cracking” correspond to regions with negative η values that mainly resulted from the severe cracking or fragmentation of the specimens during compression testing. The occurrence of dynamic strain aging during deformation can also result in low or negative values of η [35]. Although the features of the three maps are basically similar, the alteration and expansion of instability and cracking regions with increasing strain suggest that strain has an important effect on the processing maps of MM AZ91 powder compacts.

As shown in Fig. 4, all of the processing maps include two cracking regions. Both regions expand significantly with increasing strain. The increase in strain also affects the instability regions. The instability region located at higher strain rates and low deformation temperatures expands with increasing strain. However, the increase in strain has a different effect on the instability region located at lower strain rates, and this instability region shrinks toward higher deformation temperatures with increasing strain.

Fig. 4 clearly shows that the workability of nanocrystalline AZ91 Mg alloy is not good at deformation temperatures lower than or equal to 250 °C and high strain rates, and the cracking and instability regions located at this deformation window expand with increasing strain. This expansion, in turn, affects the adjacent domains with high efficiency of the power dissipation (η). At low deformation temperatures ($T \leq 200$ °C), Mg and its alloys deform essentially by basal slip and twinning, which limit their workability. Consequently, deformation of Mg alloys is normally carried out at higher temperatures. It is generally believed that additional slip systems (prismatic and pyramidal) become also active when deformation temperature is higher than 300 °C, resulting in a better workability for Mg and its alloys. Furthermore, the improvement in the workability of Mg alloys at deformation temperatures higher than 300 °C has also been proven to be associated with the occurrence of dynamic recrystallization, as the most effective restoration mechanism, at these temperatures [28,30]. In addition to dislocation slip, grain boundary sliding also contributes to the deformation of fine-grained Mg alloys. The refinement of grains to submicron sizes can significantly enhance the contribution of grain boundary sliding, and the deformation mechanism of nanocrystalline Mg alloys has been proposed as combined dislocation and grain boundary activities [36,37].

The DSC curve of MM AZ91 powder presented in Fig. 5 suggests that cracking of the specimens and the poor workability of nanocrystalline AZ91 Mg alloy at deformation temperatures higher than or equal to 400 °C is a result of the formation of a liquid phase. This liquid phase results from a eutectic reaction between the fine β -Mg₁₇Al₁₂ dispersoids and the α -Mg matrix of the MM AZ91 powder particles. As shown before in Fig. 1, the large β -Mg₁₇Al₁₂ precipitates present in the microstructure of the as-received AZ91 powder particles were no longer detectable in the microstructure of the MM AZ91 powder particles, which can be attributed to both the dissolution of the β -Mg₁₇Al₁₂ phase in the α -Mg matrix of the

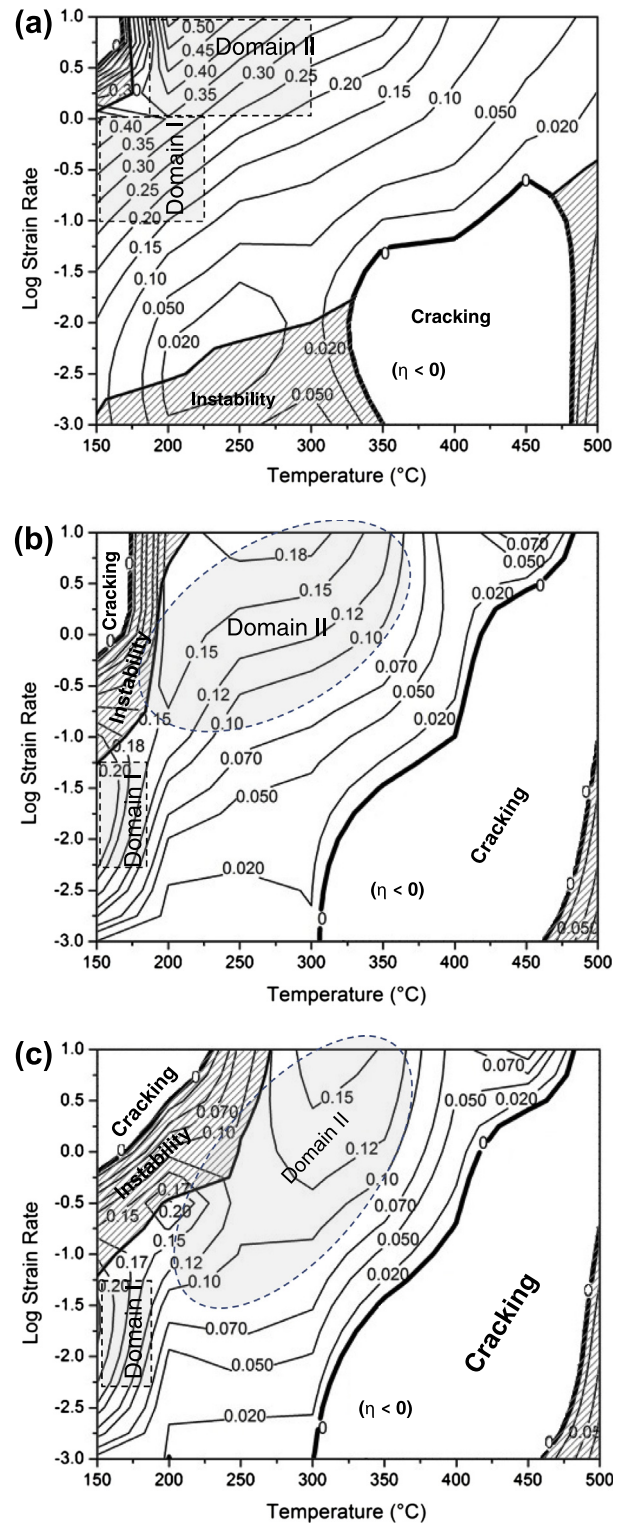


Fig. 4. Processing maps of the MM AZ91 powder compacts developed at strains of (a) 0.1, (b) 0.5, and (c) 0.8.

powder particles and the fragmentation of the large β -Mg₁₇Al₁₂ precipitates into very fine dispersoids via mechanical milling.

The values of efficiency of the power dissipation (η) obtained for the specimens deformed at moderate deformation temperatures and at strain rates less than or equal to 0.01 s⁻¹ (“Log strain rate” less than or equal to -2) were very low (200 °C $\leq T \leq 300$ °C) or even negative (300 °C $\leq T \leq 400$ °C) (Fig. 4). Low or negative values

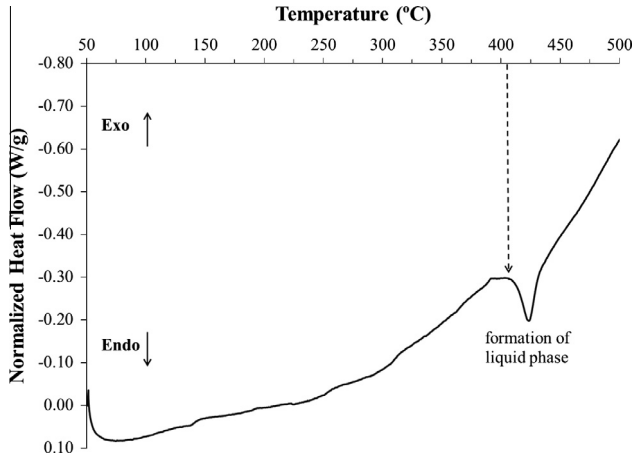


Fig. 5. Differential scanning calorimetry (DSC) curve of the MM AZ91 powder.

of the efficiency of the power dissipation (η) can be obtained under the deformation conditions promoting the interaction of mobile dislocations and solute atoms (dynamic strain aging). Such interactions are avoided at sufficiently high strain rates. Another mechanism that can lead to low or negative η values is the dynamic propagation of preexisting or newly formed cracks in the workpiece, which eventually may lead to fracture of the workpiece [35]. Due to the fact that no cracking was detected under the above-mentioned deformation window, the low and negative values of efficiency of the power dissipation (η) obtained for the specimens deformed at such low strain rates can be attributed to the occurrence of dynamic strain aging.

The processing map developed for a strain of 0.1 (Fig. 4(a)) exhibits two domains with high efficiency of the power dissipation (η). These domains are normally considered as the suitable conditions for hot deformation. However, the effect of strain on these domains is of great importance and should be studied. Fig. 4 shows that the increase in strain greatly affects domain I. Both the area and the peak efficiency of domain I decrease significantly with increasing strain, and at a strain of 0.8 (Fig. 4(c)), this domain covers only a very narrow temperature range. Considering the effect of strain on domain I, this domain cannot be recommended as a safe and suitable domain for the hot deformation of nanocrystalline AZ91 Mg alloy. In contrast to domain I, Domain II expands noticeably with increasing strain. However, strains greater than 0.5 do not show any expanding effect on this domain, and domain II is basically similar for the processing maps developed for strains of 0.5 (Fig. 4(b)) and 0.8 (Fig. 4(c)).

Considering all above, it can be concluded that the map depicting a strain of 0.8 (Fig. 4(c)) exhibits a single domain of stable flow

(Domain II) with a peak efficiency of 15% in the following temperature and strain rate ranges: 250–350 °C and 0.1–10 s⁻¹, which is considered as the appropriate hot deformation window for the processed nanocrystalline AZ91 Mg alloy. This map also contains large flow instability and cracking regions at both low and high deformation temperatures. These regions are not suitable for hot working of the nanocrystalline AZ91 Mg alloy. According to the previous studies on the hot deformation behavior of microcrystalline AZ91 Mg alloy, this alloy exhibits a single domain of good workability associated with DRX in the temperature range of 275–375 °C and at strain rates lower than 0.01 s⁻¹ [27–29]. Although the recommended temperature range for the hot deformation of nanocrystalline AZ91 Mg alloy is very similar to that for the microcrystalline counterpart, the nanocrystalline AZ91 Mg alloy can be effectively deformed at a strain rate of 10 s⁻¹, which is about 1000 times greater than that recommended for the microcrystalline alloy. The good workability of nanocrystalline AZ91 Mg alloy at high strain rates is of great industrial importance and can increase the attractiveness of this Mg alloy for demanding structural applications. Domains such as domain II that possess a high efficiency of the power dissipation (η) and good workability have generally been associated with dynamic restoration mechanisms, such as dynamic recovery and recrystallization, for microcrystalline Mg alloys [30]. However, the mechanisms involved in the deformation of a metallic alloy can significantly be affected by its grain size.

Side views of the specimens hot-compressed at different temperatures and strain rates to a strain of 0.8 are presented in Fig. 6. The specimens experienced inhomogeneous deformation (flow localization) in the instability regions and severely cracked or fragmented in the cracking regions. The nanocrystalline AZ91 Mg alloy exhibited good workability within domain II and produced crack-free, uniformly deformed specimens, suggesting that the developed processing maps successfully identified the suitable domain for hot deformation.

3.4. Deformed specimens

The cross-section microstructure of the specimen hot-compressed to a strain of 0.8 at a temperature of 300 °C and a strain rate of 10 s⁻¹ (corresponding to domain II of the developed processing maps) is shown in Fig. 7. No second phase precipitates are visible in the microstructure, and the interfaces of initial powder particles are no longer recognizable. In fact, the microstructure of deformed MM AZ91 powder compact is composed of a grey matrix with no specific microstructural feature. Some porosity is still present in the deformed microstructure. The effect of strain on the relative density of the MM AZ91 powder compacts hot-compressed at a deformation temperature of 300 °C and a strain rate of 10 s⁻¹ is

Strain Rate (S ⁻¹)	Temperature (°C)							
	150	200	250	300	350	400	450	500
0.001								
0.01								
0.1								
1								
10	Fragmented							

Fig. 6. Side views of the MM AZ91 powder compacts hot-compressed at different temperatures and strain rates to a strain of 0.8.

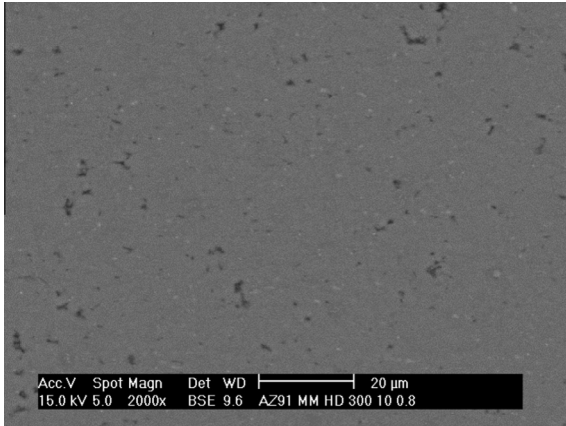


Fig. 7. Cross-section microstructure of the specimen hot-compressed at a temperature of 300 °C and a strain rate of 10 s⁻¹.

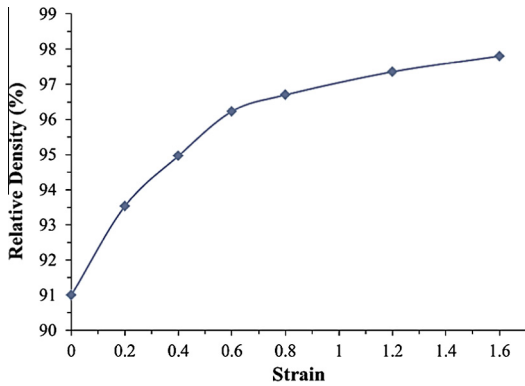


Fig. 8. Relative density of the MM AZ91 powder compacts hot-compressed at a temperature of 300 °C and a strain rate of 10 s⁻¹ as a function of strain.

illustrated in Fig. 8, implying that MM AZ91 powder compacts can be consolidated to almost full density just by open-die, uniaxial hot compression.

The XRD patterns of the MM AZ91 powder compacts hot-compressed at a strain rate of 10 s⁻¹ and at deformation temperatures of 300 °C and 350 °C (corresponding to domain II of the developed processing maps) are presented in Fig. 9. These patterns are very similar to that of the MM AZ91 powder, and the intensities of the diffraction peaks belonging to the β-Mg₁₇Al₁₂ phase are still

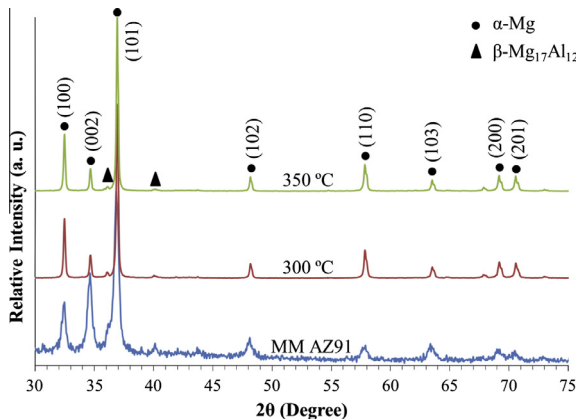


Fig. 9. The XRD patterns of the MM AZ91 powder compacts hot-compressed at a strain rate of 10 s⁻¹ and at deformation temperatures of 300 °C and 350 °C.

Table 1

Hardness values and grain sizes of some solution treated and aged AZ91 Mg alloys produced by different processing techniques.

Processing	Grain size (μm)	Hardness (HV)	Refs.
Casting	Not specified	80–100	[38]
Casting	120–150	88	[39]
Spray forming and extrusion	1–10	103	[40]
Casting and extrusion	70	85–90	[41]

very low, confirming that no significant precipitation occurs during the hot compression of nanocrystalline AZ91 Mg alloy at the above-mentioned deformation conditions. The crystallite sizes of the aforementioned powder compacts were measured to be 140 ± 10 nm using the Williamson–Hall method [33], which shows that the nanocrystalline AZ91 Mg alloy experiences some grain growth during hot deformation. However, a crystallite size of 140 nm is still considered extremely fine for Mg alloys and can result in superior mechanical properties for the consolidated materials. The hardness values of the above-mentioned MM AZ91 powder compacts were measured to be 133 ± 3 HV. This hardness value is considered very high for Mg alloys and shows an improvement of about 50% over those previously reported for bulk, heat treated AZ91 Mg alloys produced by different processing techniques (Table 1) [38–41].

4. Conclusions

This research examined the hot deformation behavior and workability characteristics of nanocrystalline AZ91 Mg alloy using hot compression tests over a wide range of deformation temperatures and strain rates and a processing map technique. The main conclusions derived from this study are the following:

1. Strain was found to have important effects on the processing maps of nanocrystalline AZ91 Mg alloy, although the processing maps developed for different strains had similar features.
2. The processing maps contained a safe domain for hot deformation in the temperature and strain rate ranges of 250–350 °C and 0.1–10 s⁻¹, which is considered as the optimum hot deformation window for nanocrystalline AZ91 Mg alloy.
3. The nanostructured AZ91 Mg alloy processed by mechanical milling showed a good thermal stability, retaining its crystallite size lower than 150 nm after the hot compression test at a temperature of 350 °C and a strain rate of 10 s⁻¹.
4. Although some porosity was still present in the microstructures of hot-compressed specimens, the hardness values of the powder compacts deformed within the safe domain for hot deformation of nanocrystalline AZ91 Mg alloy (domain II) were measured to be about 133 HV.

Acknowledgments

The authors would like to thank the Comunidad de Madrid for their financial support of this work through the ESTRUMAT Grant #S2009/MAT-1585.

References

- [1] E.F. Volkova, *Met. Sci. Heat Treat.* 48 (2006) 473–478.
- [2] Y. Li, Y. Chen, H. Cui, J. Ding, L. Zuo, J. Zhang, *Rare Met.* 28 (2009) 91–97.
- [3] S.J. Liang, Z.Y. Liu, E.D. Wang, *Mater. Lett.* 62 (2008) 3051–3054.
- [4] K. Kubota, M. Mabuchi, K. Higashi, *J. Mater. Sci.* 34 (1999) 2255–2262.
- [5] R.B. Figueiredo, T.G. Langdon, *Scr. Mater.* 61 (2009) 84–87.
- [6] O. Sitdikov, R. Kaibyshev, *Mater. Trans.* 42 (2001) 1928–1937.

- [7] S.M. Fatemi-Varzaneh, A. Zarei-Hanzaki, H. Beladi, *Mater. Sci. Eng., A* 456 (2007) 52–57.
- [8] S.W. Xu, S. Kamado, N. Matsumoto, T. Honma, Y. Kojima, *Mater. Sci. Eng., A* 527 (2009) 52–60.
- [9] Y. Xu, L. Hu, Y. Sun, *J. Alloys Comp.* 580 (2013) 262–269.
- [10] A. Galiyev, R. Kaibyshev, T. Sakai, *Mater. Sci. Forum* 419–422 (2003) 509–514.
- [11] B.-J. Lv, J. Peng, Y.-J. Wang, X.-Q. An, L.-P. Zhong, A.-T. Tang, F.-S. Pan, *Mater. Des.* 53 (2014) 357–365.
- [12] L. Li, M.O. Lai, M. Gupta, B.W. Chua, A. Osman, *J. Mater. Sci.* 35 (2000) 5553–5561.
- [13] M.O. Lai, L. Lu, W. Laing, *Compos. Struct.* 66 (2004) 301–304.
- [14] J. Liu, C. Suryanarayana, D. Ghosh, G. Subhash, *L. An, J. Alloys Comp.* 563 (2013) 165–170.
- [15] N. Cui, P. He, J.L. Luo, *Acta Mater.* 47 (1999) 3737–3743.
- [16] H. Imamura, K. Masanari, M. Kusuhara, H. Katsumoto, T. Sumi, Y. Sakata, *J. Alloys Comp.* 386 (2005) 211–216.
- [17] M. Anik, F. Karanfil, N. Küçükdeveci, *Int. J. Hydrogen Energy* 37 (2012) 299–308.
- [18] S. Hwang, C. Nishimura, P.G. McCormick, *Mater. Sci. Eng., A* 318 (2001) 22–33.
- [19] P. Cao, L. Lu, M.O. Lai, *Mater. Res. Bull.* 36 (2001) 981–988.
- [20] B. Zheng, O. Ertorer, Y. Li, Y. Zhou, S.N. Mathaudhu, C.Y.A. Tsao, E.J. Lavernia, *Mater. Sci. Eng., A* 528 (2011) 2180–2191.
- [21] F. Wen-bin, F. Wa, S. Hong-fei, *Powder Technol.* 212 (2011) 161–165.
- [22] M.A. Jabbari Taleghani, J.M. Torralba, *Mater. Lett.* 98 (2013) 182–185.
- [23] M. Wolff, T. Ebel, M. Dahms, *Adv. Eng. Mater.* 12 (2010) 829–836.
- [24] C. Zubizarreta, S. Giménez, J.M. Martín, I. Iturriza, *J. Alloys Comp.* 467 (2009) 191–201.
- [25] G. Chunlei, X. Yongdong, W. Mengjun, *Mater. Sci. Eng., A* 528 (2011) 4199–4203.
- [26] K. Ishikawa, H. Watanabe, T. Mukai, *Mater. Lett.* 59 (2005) 1511–1515.
- [27] M. Mu, Z. Zhi-min, Z. Bao-hong, D. Jin, *J. Alloys Comp.* 513 (2012) 112–117.
- [28] M.A. Jabbari Taleghani, J.M. Torralba, *Mater. Sci. Eng., A* 580 (2013) 142–149.
- [29] Y. Xu, L. Hu, Y. Sun, *Mater. Sci. Eng., A* 578 (2013) 402–407.
- [30] N. Srinivasan, Y.V.R.K. Prasad, P. Rama Rao, *Mater. Sci. Eng., A* 476 (2008) 146–156.
- [31] J.-Y. Li, J.-X. Xie, J.-B. Jin, Z.-X. Wang, *T. Nonferr, Met. Soc.* 22 (2012) 1028–1034.
- [32] E. Cerri, P. Leo, P.P. De Marco, *J. Mater. Process. Technol.* 189 (2007) 97–106.
- [33] G.K. Williamson, W.H. Hall, *Acta Metall.* 1 (1953) 22–31.
- [34] C. Suryanarayana, *Prog. Mater. Sci.* 46 (2001) 1–184.
- [35] G.E. Dieter, H.A. Kuhn, S.L. Semiatin, *Handbook of Workability and Process Design*, ASM International, Materials Park, Ohio, United States of America, 2003.
- [36] S. Hwang, P. McCormick, *Met. Mater.* 4 (1998) 543–547.
- [37] H. Diao, C. Yan, J.M. Bell, L. Lu, G.P. Zhang, S. Kabra, K.D. Liss, M.W. Chen, *Mater. Technol.* 27 (2012) 85–87.
- [38] S. Celotto, *Acta Mater.* 48 (2000) 1775–1787.
- [39] C.H. Cáceres, C.J. Davidson, J.R. Griffiths, C.L. Newton, *Mater. Sci. Eng., A* 325 (2002) 344–355.
- [40] Y. Li, Y. Chen, H. Cui, B. Xiong, J. Zhang, *Mater. Charact.* 60 (2009) 240–245.
- [41] M. Thirumurugan, S. Kumaran, *T. Nonferr, Met. Soc.* 23 (2013) 1595–1601.